Evolution of Microstructures and Compressive Properties in $Al_{0.5}CrFeNi_{2.1}Mn_{0.8}Ti_x$ High Entropy Alloys

Xu Chen[1,2] · Di Gao[1,2] · Yan Zhang[1,2] · Jia Xuan Hu[1,2] · Ye Liu[1,2] · Feng Xiang[3]

Abstract

The effects of Ti on the microstructures, macrohardness and compressive properties of the as-cast $Al_{0.5}CrFeNi_{2.1}Mn_{0.8}Ti_x$ HEAs were investigated. The results showed that the microstructures of as-cast $Al_{0.5}CrFeNi_{2.1}Mn_{0.8}Ti_x$ alloys was changed from FCC phase to a mixture of FCC and BCC phases, then to a mixture of BCC phase and Ti-containing intermetallic compound as the increasing of Ti content. Chrysanthemum-like eutectic microstructure was obtained in the $Al_{0.5}CrFeNi_{2.1}Mn_{0.8}Ti_{0.5}$ and $Al_{0.5}CrFeNi_{2.1}Mn_{0.8}Ti$ alloys. The area of flower core was composed of BCC2 phase, and eutectic microstructure was achieved in the petal area which contained BCC1 phase and BCC2 phase. Moreover, the macrohardness of the as-cast alloys increased with the increasing of Ti, and the $Al_{0.5}CrFeNi_{2.1}Mn_{0.8}Ti_{0.5}$ alloy showed excellent comprehensive compressive properties.

Keywords Evolution · Microstructure · Compressive property · $Al_{0.5}CrFeNi_{2.1}Mn_{0.8}Ti_x$ HEAs

1 Introduction

According to the traditional alloys design concept, adding too much alloying elements to conventional alloys could be easy to form brittle intermetallic compounds which would worsen the performance [1–3]. It is generally believed that the large entropy value in high entropy alloys (HEAs) due to the large variety of alloying elements result in the high entropy effect which could inhibit the formation of intermetallic compounds [4–6]. HEAs designed by novel way which are commonly composed of simple solid solution greatly broaden the variety of alloys and also have great potential in many applications [7–13].

Traditional titanium alloy is widely used in the field of aerospace. In addition, Ti element is often added into HEAs to regulate microstructure and improve their performance. Wang et al. [14]. studied the effects of Ti on the microstructure and properties of AlCrFeCoNiCu alloy. It was found that the addition of Ti changes the morphology of the alloy from dendrites to cellular crystals, and the hardness increases while the plasticity decreases. He et al. [15]. prepared the HEA coating by laser cladding method, and the effect of Ti element on the structure and properties of FeCoCrNiAlTi HEA coating was studied. The results showed that the HEA coating consists of two BCC phases, the hardness of the alloy increased while the wear resistance coefficient decreased. So far most of the widely studied AlCrFeNi-M HEAs contain Co element. However, the application of Co-containing HEA in modern industry is restricted because of its high price. It is common know that Mn element is cheap and abundant in natural world. Based on the AlCrCuFeCoNi alloy, new alloy was introduced in which Co was replaced by Mn. Chen et al. [16]. found that the addition of Mn promotes the formation of BCC phase in the Co-free HEA. Appropriate amount of Mn was added to the alloy could improve the mechanical property of the alloy [17]. Therefore, based on the $AlCoCrFeNi_{2.1}$ high entropy alloy with

✉ Xu Chen
  chenxusun@163.com

✉ Ye Liu
  liuye216@163.com

1   Key Laboratory of Materials Design and Preparation Technology of Hunan Province, School of Materials Science and Engineering, Xiangtan University, Xiangtan 411105, People's Republic of China

2   Hunan Provincial Key Laboratory of Thin Film Materials and Devices, School of Materials Science and Engineering, Xiangtan University, Xiangtan 411105, People's Republic of China

3   Hunan Provincial Key Laboratory of Vehicle Power and Transmission System, Hunan Institute of Engineering, Xiangtan 411104, People's Republic of China

excellent mechanical properties [18], $Al_{0.5}CrFeMn_{0.8}Ni_{2.1}Ti_x$ high entropy alloys were obtained by replacing the Co with Mn and adding Ti element in this investigation. In order to provide reliable data for the practical application of the $Al_{0.5}CrFeMn_{0.8}Ni_{2.1}Ti_x$ alloys, the effect of Ti element on the microstructure, hardness and compression properties was researched systematically by means of X-ray diffractometer, optical microscope, scanning electron microscopy-energy spectrometer, hardness tester and electro-hydraulic servo pressure testing machine.

2 Experiment

The experimental granular metals of Al, Cr, Fe, Mn, Ni and Ti with purities above 99.99% were used as raw materials, which were prepared by the molar ratio of 0.5:1.0:1.0:0.8:2.1:x ($x = 0$, 0.5, 1.0 and 1.5). The nominal composition of the $Al_{0.5}CrFeMn_{0.8}Ni_{2.1}Ti_x$ alloys was shown in Table 1. The alloys were melted in a WK non-consumable vacuum arc furnace under argon protection, and the weight of cast ingot was about 15 g. The ingots of the alloys were melted repeated at least 5 times to improve the chemical homogeneity. Moreover, the samples for microstructure observation and performance testing were cut from the centre of the ingots.

The phase composition and microstructure of the $Al_{0.5}CrFeMn_{0.8}Ni_{2.1}Ti_x$ alloys were observed by an AJSM-6360LV scanning electron microscope with energy spectrometer. The surfaces of the samples were etched with aqua regia before the observation with scanning electron microscope. The phase structure of the alloys was analyzed by a Rigaku UItimate IV X-ray diffractometer, and the diffraction angle ranged from 20° to 90° and the scanning speed was 5°/min. The macrohardness of the alloy was measured by an EVERONE MH-5L vickers hardness tester with a loading load of 1 kg and a loading time of 15 s, and at least 8 points were measured for each sample to improve the accuracy. The compressed samples were 6 mm in diameter and 9 mm in height giving an aspect ratio of 1:1.5. The surfaces of the cylindrical compression sample were polished carefully to obtain smooth surfaces. A Gleeble-3500 thermomechanical simulator was used to carry out the compression tests at a nominal strain rate of 5×10^{-4} s^{-1} under room temperature.

3 Results

3.1 XRD Analysis

The XRD patterns of as-cast $Al_{0.5}CrFeNi_{2.1}Mn_{0.8}Ti_x$ alloys were shown in Fig. 1. Only the diffraction peaks that corresponding to FCC phase in as-cast Ti_0 alloy were found, as can be seen in Fig. 1a. However, two kinds of BCC phases were formed as the content of Ti increased to 0.5 and the

Table 1 Nominal chemical composition of $Al_{0.5}CrFeMn_{0.8}Ni_{2.1}Ti_x$ high entropy alloys (at%)

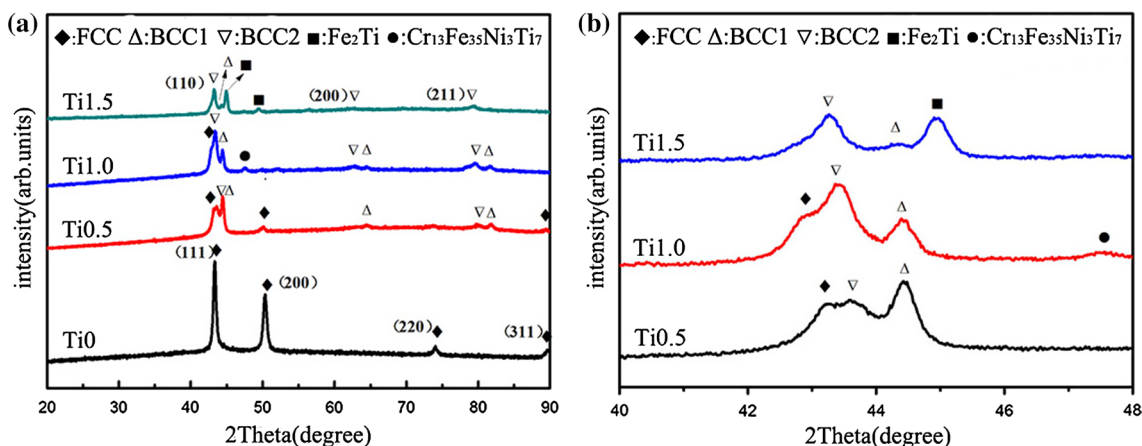| Alloys	Abbreviation	Al	Cr	Mn	Fe	Ni	Ti
$Al_{0.5}CrFeMn_{0.8}Ni_{2.1}$	Ti_0	9.26	18.52	14.81	18.52	38.89	–
$Al_{0.5}CrFeMn_{0.8}Ni_{2.1}Ti_{0.5}$	$Ti_{0.5}$	8.47	16.95	13.56	16.95	35.59	8.47
$Al_{0.5}CrFeMn_{0.8}Ni_{2.1}Ti_{1.0}$	$T_{1.0}$	7.8	15.63	12.5	15.63	32.81	15.63
$Al_{0.5}CrFeMn_{0.8}Ni_{2.1}Ti_{1.5}$	$Ti_{1.5}$	7.25	14.49	11.59	14.49	30.43	21.74

Fig. 1 XRD patterns of as-cast $Al_{0.5}CrFeNi_{2.1}Mn_{0.8}Ti_x$ alloys (**a**) and details shift of the XRD peaks (**b**)

BCC phases were marked as BCC1 phase and BCC2 phase respectively. Therefore, there were FCC phase, BCC1 phase and BCC2 phase in the as-cast $Ti_{0.5}$ alloy. Although the diffraction peaks of FCC phase were weak when the content of Ti increased to 1.0, the FCC phase was obtained in the alloy. In addition, there was only a weak diffraction peak of other phase rather than the above-mentioned phases when 2θ was 47° in the $Ti_{1.0}$ alloy. According to the analysis by comparing with standard PDF card, the phase was supposed to be $Cr_{13}Fe_{35}Ni_3Ti_7$ phase. The diffraction peaks of FCC phase were not obtained and a weak diffraction peak of BCC1 phase appeared in the as-cast $Ti_{1.5}$ alloy, as shown in Fig. 1a. Therefore, the main phase was BCC2 phase in the alloy. In addition, it should be noted that a kind of intermetallic compound, Fe_2Ti phase, was also formed besides the above mentioned solid solution. As the increasing of Ti content, the as-cast microstructure of $Al_{0.5}CrFeNi_{2.1}Mn_{0.8}Ti_x$ alloys changed from FCC phase to FCC phase and BCC phase, and then to the mixture of BCC phase and Ti-containing intermetallic compound. Details shift of the XRD peaks in the as-cast $Al_{0.5}CrFeNi_{2.1}Mn_{0.8}Ti_x$ alloys were shown in Fig. 1b, which indicated that the lattice constant increased with the increasing of Ti content due to the fact that the

(111) diffraction peaks in FCC phase and (110) in BCC phase shifted towards lower angle side gradually.

3.2 Microstructure Analysis

The optical microscope images of as-cast $Al_{0.5}CrFeNi_{2.1}Mn_{0.8}Ti_x$ alloys were shown in Fig. 2. It could be seen that the morphology of Ti_0 alloy was dendritic, and with the increasing of Ti the morphology of the alloys changed from dendritic to equiaxed crystal. Equiaxed grains were observed in the $Ti_{0.5}$, $Ti_{1.0}$ and $Ti_{1.5}$ alloys. Moreover, the grain size increased gradually as the Ti content increased from 0.5 to 1.5.

The scanning electron microscope images and the chemical composition in corresponding region of the as-cast $Al_{0.5}CrFeNi_{2.1}Mn_{0.8}Ti_x$ alloys were show in Fig. 3 and Table 2, respectively. Combined with the XRD patterns (Fig. 1) and the energy spectrum analysis (Table 2), it could be referred that the region F_0 was the FCC phase and the region β_0 was the BCC1 phase in Ti_0 alloy as shown in Fig. 3a. The BCC1 phase was not detected in XRD pattern due to the content was relatively low. The chrysanthemum-like microstructure appeared in the $Ti_{0.5}$ and $Ti_{1.0}$ alloys as
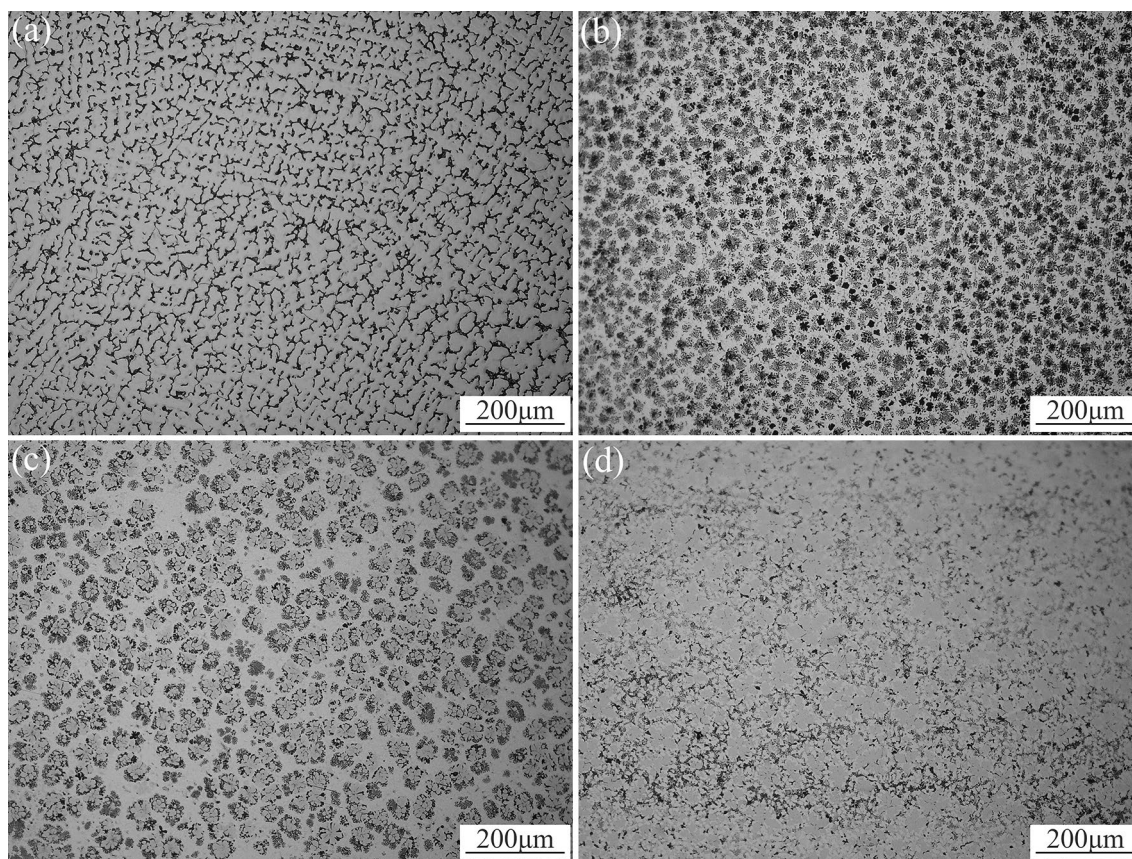

Fig. 2 Optical microscope (OM) images of as-cast $Al_{0.5}CrFeNi_{2.1}Mn_{0.8}Ti_x$ alloys. a Ti_0 alloy; b $Ti_{0.5}$ alloy; c $Ti_{1.0}$ alloy; d $Ti_{1.5}$ alloy

Fig. 3 Scanning electron microscope (SEM) images of as-cast $Al_{0.5}CrFeNi_{2.1}Mn_{0.8}Ti_x$ alloys. **a** Ti_0 alloy; **b** $Ti_{0.5}$ alloy; **c** $Ti_{1.0}$ alloy; **d** $Ti_{1.5}$ alloy
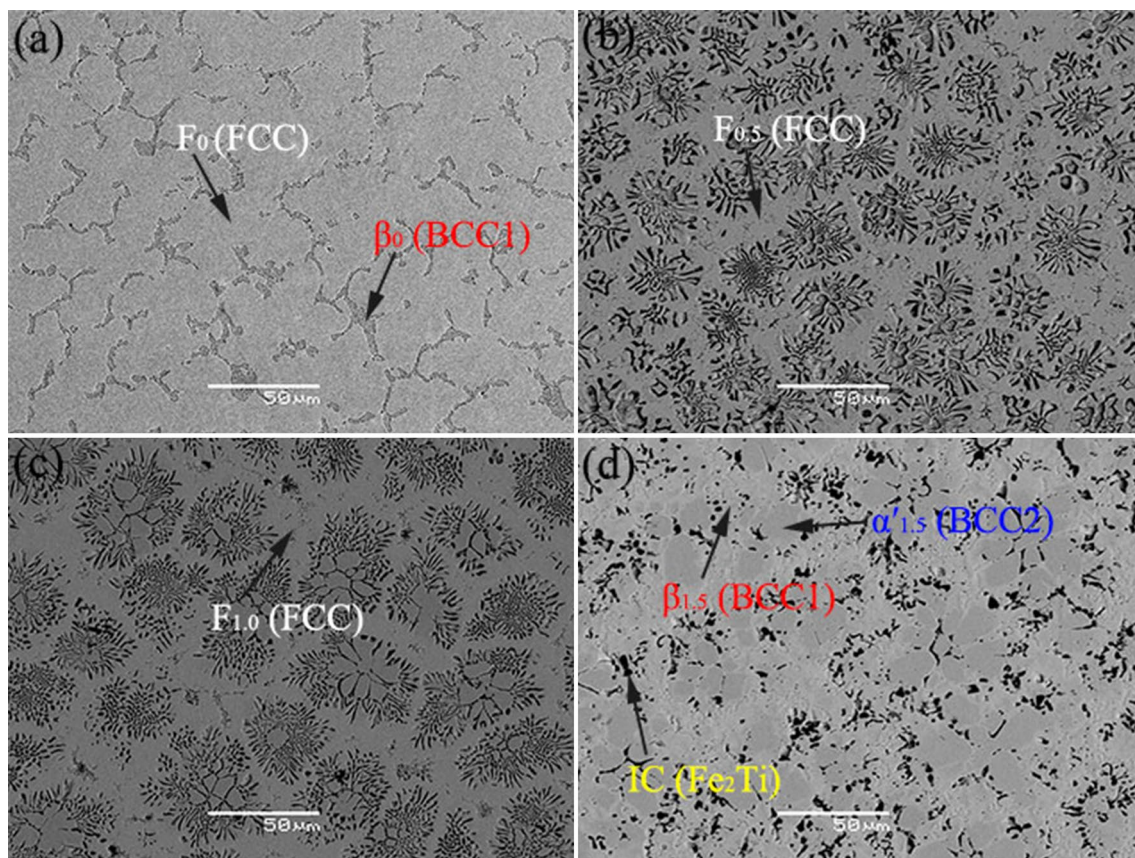
Table 2 Chemical composition in different regions of as-cast $Al_{0.5}CrFeNi_{2.1}Mn_{0.8}Ti_x$ alloys

Alloys	Region	Structure	Al	Ti	Cr	Mn	Fe	Ni
Ti_0	F_0	FCC	7.11	–	22.47	11.99	23.47	34.96
	β_0	BCC1	20.20	–	7.38	19.23	7.96	45.23
$Ti_{0.5}$	$F_{0.5}$	FCC	3.19	8.39	16.37	13.72	22.68	35.66
	$\alpha_{0.5}$	BCC2	10.44	13.22	15.24	12.51	14.51	34.01
	$\beta_{0.5}$	BCC1	5.8	8.47	21.86	12.05	18.27	33.55
$Ti_{1.0}$	$F_{1.0}$	FCC	2.65	18.23	9.71	16.6	17.3	35.36
	$\alpha'_{1.0}$	BCC2	20.60	18.20	5.29	6.68	7.97	41.27
	$\alpha_{1.0}$	BCC2	19.0	18.62	3.57	6.99	8.88	42.8
	$\beta_{1.0}$	BCC1	1.5	11.42	28.60	11.73	20.63	26.29
$Ti_{1.5}$	$\alpha'_{1.5}$	BCC2	17.11	24.80	3.56	5.27	9.16	40.10
	$\beta_{1.5}$	BCC1	1.28	25.61	16.50	12.37	22.20	22.04
	IC	Fe₂Ti	9.02	26.66	3.43	7.21	8.21	45.56

illustrated in Figs. 3b, c and 4, moreover, the chrysanthemum-like microstructure had flower core portions in the $Ti_{1.0}$ alloy rather than the $Ti_{0.5}$ alloy. The SEM-EDS maps of the $Ti_{1.0}$ alloy were shown in Fig. 5 and the segregation of elements was obtained. The elements of Cr and Fe were mainly segregated in BCC1 phase and the FCC phase was mainly enriched in Mn and Fe, however, the BCC2 phase was enriched in Al and Ni. It should be noted that the element of Ti was mainly segregated in FCC and BCC2 phases, while the content of Ti was relatively low in the BCC1 phase. As the increasing of Ti, the chrysanthemum-like microstructure disappeared in the $Ti_{1.5}$ alloy. According to the XRD analysis and energy spectrum analysis, the dark gray region $\alpha'_{1.5}$ was BCC2 phase, the light gray region $\beta_{1.5}$ was BCC1 phase,
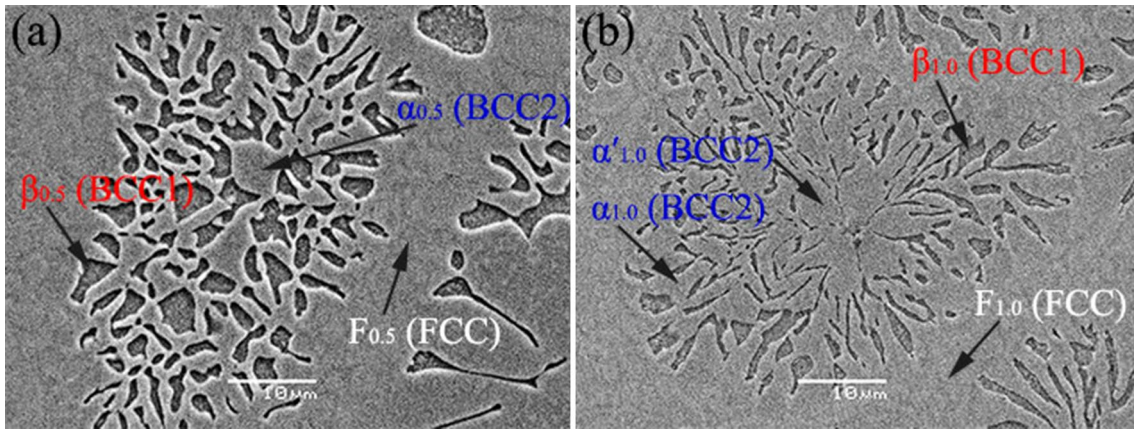
Fig. 4 High-magnification SEM images of chrysanthemum-like microstructure in $Ti_{0.5}$ alloy (**a**) and $Ti_{1.0}$ alloy (**b**)
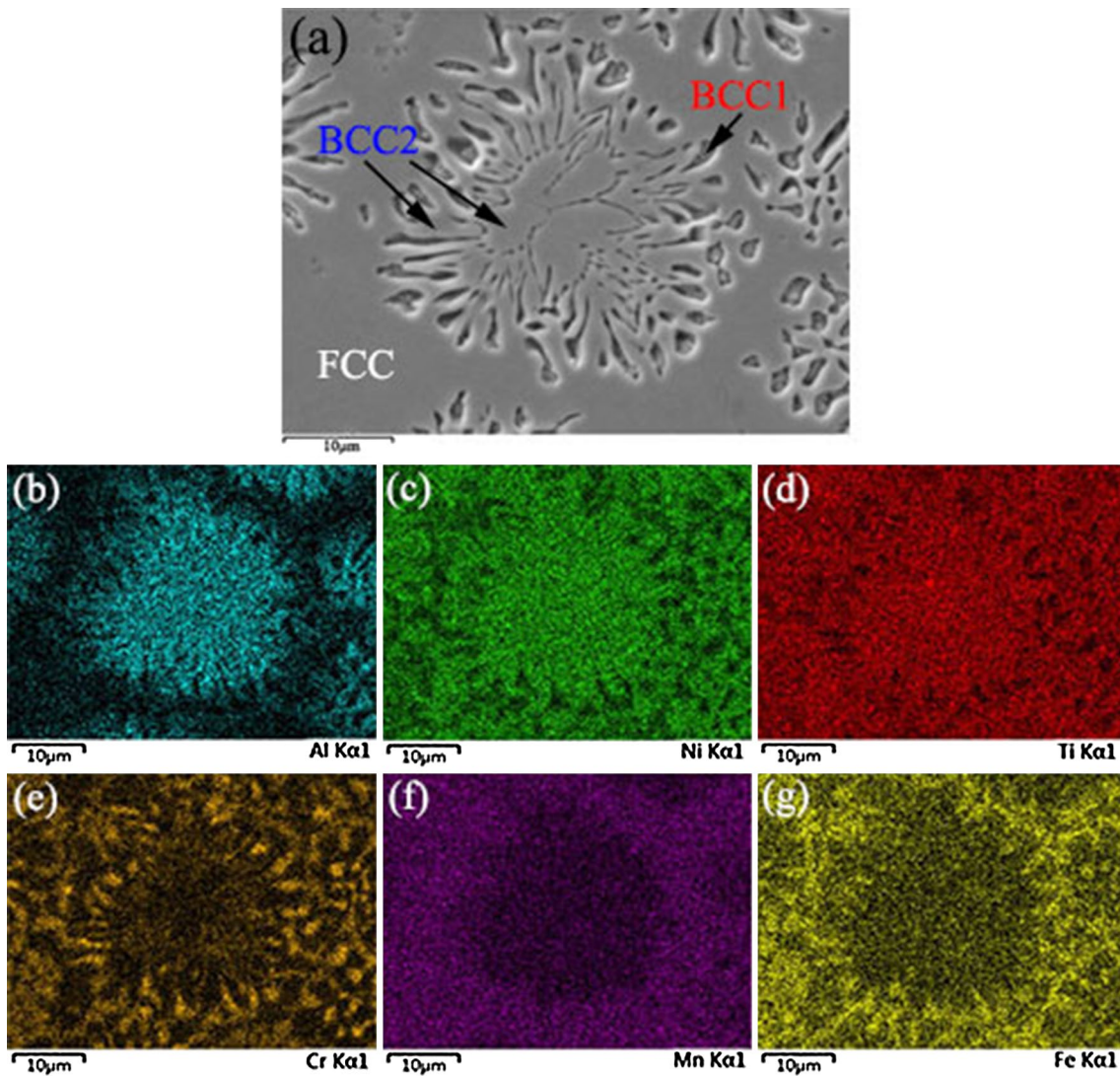

Fig. 5 SEM-EDS maps of $Al_{0.5}CrFeMn_{0.8}Ni_{2.1}Ti_{1.0}$ alloy ($Ti_{1.0}$ alloy). **a** SEM; **b** Al; **c** Ni; **d** Ti; **e** Cr; **f** Mn; **g** Fe

and the black region *IC* was Fe_2Ti intermetallic compound presented on grain boundary as shown in Fig. 3d.

Figure 4 showed the high magnification SEM images of chrysanthemum-like microstructure in $Ti_{0.5}$ and $Ti_{1.0}$ alloys. Combined with energy spectrum analysis and XRD analysis, it could be found that in the $Ti_{0.5}$ alloy as shown in Fig. 4a, the region $F_{0.5}$ was the FCC phase, and the region $\alpha_{0.5}$ and region $\beta_{0.5}$ constituted the petal, what is more, the region $\alpha_{0.5}$ was the BCC2 phase, the region $\beta_{0.5}$ was the BCC1 phase. In the $Ti_{1.0}$ alloy as shown in Fig. 4b, the region $F_{1.0}$ was the FCC phase, the region $\alpha'_{1.0}$ was the flower core portion, and the region $\alpha_{1.0}$ and the region $\beta_{1.0}$ constitute the petal, wherein the regions of $\alpha'_{1.0}$ and $\alpha_{1.0}$ were the BCC2 phase, and the region $\beta_{1.0}$ was the BCC1 phase.

3.3 Macrohardness and Compression Performance

Macrohardness of the as-cast $Al_{0.5}CrFeNi_{2.1}Mn_{0.8}Ti_x$ alloys was shown in Fig. 6a and the macrohardness increased gradually as the increasing of Ti. The macrohardness of Ti-free $Al_{0.5}CrFeNi_{2.1}Mn_{0.8}$ alloy was only about 182Hv, while the macrohardness sharply increased to 526Hv in the $Ti_{0.5}$ alloy. However, the increment rate of macrohardness was decreased when the content of Ti continued to increase. The macrohardness of the $Ti_{1.0}$ alloy was about 650Hv and the macrohardness reached to 700Hv in the $Ti_{1.5}$ alloy. The engineering compressive stress–strain curves of the as-cast $Al_{0.5}CrFeMn_{0.8}Ni_{2.1}Ti_x$ alloy were shown in Fig. 6b, and Table 3 presented the relevant data of the compression properties of the alloys. It should be noted that the compressive strain to fracture of the Ti_0 alloy higher than 15% and remains unbroken under the experimental condition, indicating the plasticity was relatively good. The plasticity of the alloys decreased gradually as the increasing of Ti content. The compressive strain to fracture of the $Ti_{0.5}$, $Ti_{1.0}$ and $Ti_{1.5}$ alloys were 5.6%, 1.7% and 0%, and the corresponding compressive maximum stress were 1523 MPa, 1336 MPa and

Table 3 Summary of engineering compressive maximum stress and compressive strain to fracture for as-cast $Al_{0.5}CrFeNi_{2.1}Mn_{0.8}Ti_x$ alloys

Alloys	Maximum stress (MPa)	Compressive strain to fracture (%)
Ti_0	> 1400	> 15
$Ti_{0.5}$	1523	5.6
$Ti_{1.0}$	1336	1.7
$Ti_{1.5}$	167	≈ 0

167 MPa, respectively. $Ti_{0.5}$ alloy exhibited excellent comprehensive compression resistance resulted from the good combination of compressive maximum stress and compressive strain to fracture. The deformation mechanism of $Ti_{1.0}$ alloy was mainly dominated by elastic deformation, and only a small amount of plastic deformation occurred during the process of fracture. The compressive maximum stress and compressive strain to fracture of the $Ti_{1.0}$ alloy were lower than that of $Ti_{0.5}$ alloy. The compressive maximum stress and compressive strain to fracture of the $Ti_{1.5}$ alloy were extremely low compared with other alloys, indicating the alloy was brittle.

4 Discussion

4.1 The Effect of Ti on Microstructure

It was widely know that HEAs had many components which resulted in the tendency to form solid solutions with simple structures unlike conventional alloys. Basing on the H-R criterion of traditional alloys and a large number of experimental results, empirical formulas were proposed to describe the conditions forming stable solid solution and the condition which structure of the phase tended to form in HEAs
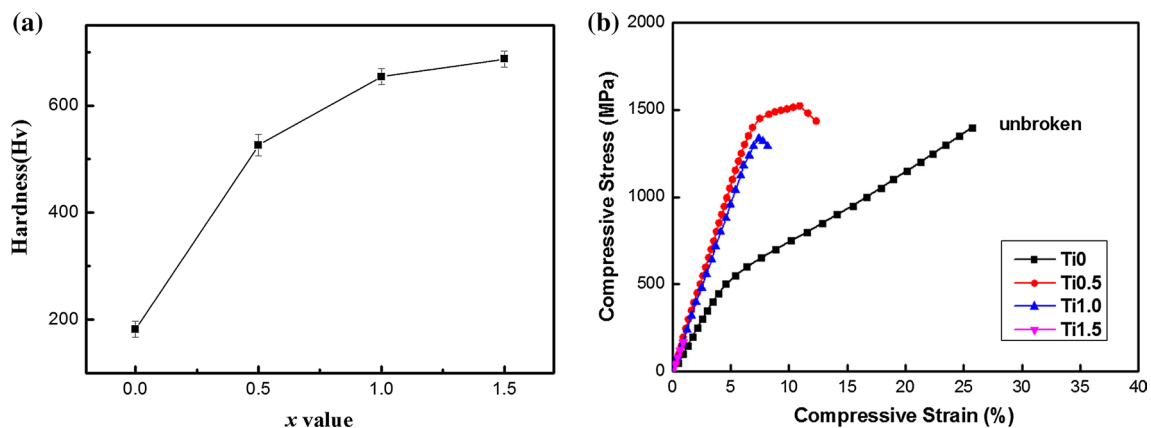

Fig. 6 The macrohardness (**a**) and the engineering compressive stress–strain curves (**b**) of as-cast $Al_{0.5}CrFeNi_{2.1}Mn_{0.8}Ti_x$ alloys

[19–22]. Previous experimental results showed that phase structure in HEAs was predicted effectively by those empirical parameters, moreover, the experimental efficiency was improved greatly [21, 22]. The condition of HEAs could forming solid solution were as following: mixing entropy (ΔS_{mix}) greater than 12 J/K mol and less than 17.5 J/K mol, mixing enthalpy (ΔH_{mix}) greater than or equal to −20 kJ/mol and less than or equal to 5 kJ/mol, thermodynamic parameters $\Omega \geq 1.1$, atomic-size difference (δ)≤6.6. The valence electron concentration (*VEC*) of the alloy system could be used to predict the condition that the FCC solid solution or BCC solid solution was tended to form in HEAs. Mixed microstructure of FCC and BCC phases had a tendency to form when $6.87 \leq VEC \leq 8.0$. Only simple FCC solid solution would be obtained when $VEC > 8.0$, while the BCC structure formed when $VEC < 6.87$.

ΔS_{mix} and Ω of the $Al_{0.5}CrFeNi_{2.1}Mn_{0.8}Ti_x$ alloys satisfied the conditions for forming solid solution, as shown in Table 4. ΔH_{mix} and δ of the alloys satisfied the conditions for forming solid solution except for the $Ti_{1.5}$ alloy. Moreover, the ΔH_{mix} of $Ti_{1.5}$ alloy was − 21.11 kJ/mol and the δ was 6.63 which were close to the critical value, indicating that the alloy not only had solid solution, but also intermetallic compound. The *VEC* of the alloys satisfied the range of $6.87 \leq VEC \leq 8.0$ as shown in Table 4, indicating that the alloys tended to obtain the mixed microstructure of FCC and BCC solid solutions. It should be noticed that the *VEC* of the $Ti_{1.5}$ alloy was 6.97, which was close to the critical value of 6.87. The results of prediction illustrated that BCC phase could exist stably in $Ti_{1.5}$ alloy rather than the FCC phase. The predictions of the empirical parameters were basically in agreement with the experimental results.

According to the above analysis, the addition of Ti element promoted the formation of BCC phase. Moreover, the diffraction peaks of the alloys moved to the left resulted from the fact that the lattice constant of the alloys increased with the increasing of Ti due to the large atomic radius of Ti element. The diffraction angles that corresponding diffraction peaks of the BCC2 phase was smaller than that of the BCC1 phase indicated the lattice constant of the BCC2 phase was higher than that of the BCC1 phase. The change of the grain morphology of the alloys probably was related to the change

of the region of constitutional supercooling caused by the addition of Ti element. The generation and extent of the constitutional supercooling depended on the distribution of solute mass concentration in the front of liquid–solid interface and the distribution of actual temperature. The effect of mass fraction, casting temperature gradient and casting solidification speed on crystal growth was researched widely [21]. The crystal growth was dominated by the mass fraction of the alloys when temperature gradient and solidification rate were constant. Furthermore, the crystal morphologies of the alloys changed from dendritic crystal to equiaxed crystal as the mass fraction of solute increased. It could be speculated that the solute concentration in the front of solid–liquid interface was redistribution with the increasing of Ti content, causing the change of the constitutional supercooling region, thus affecting the microstructure of the investigated alloys.

4.2 The Formation of Chrysanthemum-Like Microstructure

The microstructure of the Ti_0 alloy was mainly composed of FCC phase. Compared with the Ti_0 alloy, the content of the FCC phase was reduced while the BCC phase appeared eutectic microstructure consisting of BCC1 phase and BCC2 phase was obtained in $Ti_{0.5}$ alloy. The eutectic microstructure was also formed after the formation of the proeutectic BCC2 phase in the $Ti_{1.0}$ alloy. Thus, the formation process of the chrysanthemum-like microstructure could be speculated as follows: The $Ti_{0.5}$ alloy with the eutectic composition started to solidify as temperature decreased gradually. Under the condition of rapid cooling which resulted in the corresponding non-equilibrium solidification, the eutectic temperature was achieved firstly, and at the same time chrysanthemum-like eutectic microstructure appeared radial pattern which was composed of BCC1 phase and BCC2 phase formed. As the temperature further reduced, an FCC phase formed which originated from the remaining liquid phase between the dendritic regions. In the $Ti_{1.0}$ alloy, primary phase (BCC2 phase) was obtained firstly as the decreasing of temperature. Moreover, the BCC2 phase was located at the stamen area of the chrysanthemum-like eutectic microstructure, as shown in Fig. 3c. With the further decreasing of temperature, the eutectic microstructure was formed around the primary phase and then the remaining liquid translated into the FCC phase. In the $Ti_{1.5}$ alloy, the BCC2 phase was dominated. In addition, the eutectic microstructure disappeared and a small amount of BCC1 phase was achieved at grain boundary. It should be speculated that the disappearance of the eutectic microstructure might be related to divorced eutectic. The $Ti_{1.5}$ alloy was supposed to be a hypereutectic alloy and there was a large number of BCC2 phase while the content of eutectic microstructure was less.

Table 4 Empirical thermodynamic parameters and structural factor parameters of as-cast $Al_{0.5}CrFeNi_{2.1}Mn_{0.8}Ti_x$ alloys

Alloy	ΔH_{mix} (kJmol^{-1})	ΔS_{mix} (JK^{-1} mol^{-1})	Ω	δ (%)	VEC
Ti_0	− 10.01	12.42	2.13	3.92	7.80
$Ti_{0.5}$	− 15.26	13.78	1.57	5.40	7.47
$Ti_{1.0}$	− 18.37	14.08	1.34	6.18	7.20
$Ti_{1.5}$	− 21.11	14.07	1.18	6.63	6.97

Furthermore, the characteristics of the eutectic structure presented chrysanthemum-like disappeared due to the fact that the BCC2 phase formed in the eutectic microstructure was attached to the primary BCC2 phase while a few BCC1 phase solidified finally at the grain boundary. In addition, the increased Ti content was out of the solid solubility resulted in the formation of Ti-containing intermetallic compound.

4.3 The Effect of Ti on Macrohardness and Compression Performance

The macrohardness of the Ti_0 alloy was relatively low because the FCC phase was dominated while only a small amount of BCC1 phase existed in this alloy. With the increasing of Ti content, the macrohardness of the alloys increased greatly which was associated with that BCC phase was dominated gradually and the content of FCC phase was decreased. Fe_2Ti intermetallic compound with great brittle and hardness appeared in the $Ti_{1.5}$ alloy leaded to the further increasing in the macrohardness of the alloys. In addition, solid solution strengthening effect was enhanced due to the large lattice distortion resulted from the large difference of atomic radius between Ti and other elements in the alloys.

Generally, VEC was employed to determine which kinds of solid solutions could form in HEAs [23]. Besides, it was reported that intrinsically ductile refractory HEAs could be designed by manipulating VEC through controlled alloying [24]. The critical strain for the shear instability and the corresponding intrinsic failure mode of the alloys could be tuned due to the fact to some extent that alloying additions shifted the Fermi level [25]. According to the theoretical analysis and available experimental results, it had been proved that the decreasing of VEC was benefited to the improvement of the ductility of the refractory alloys [22, 24]. Guo et al. [24]. found that all the ductile refractory HEAs had a value of VEC less than 4.4, while all the brittle HEAs had a value of VEC more than 4.6 based on the database of Hf/Mo-containing HEAs. Similar phenomenon was also obtained in the Nb-containing HEAs [26, 27]. With the decreasing of VEC

from 5.21 in NbTaVW alloy to 4.72 in NbTaTiVW alloy, the ductility of the NbTaTiVW alloy increased sharply compared that of NbTaVW alloy. However, it should be noticed that only single-phase BCC solid solution was formed in the above mentioned Hf/Mo/Nb-containing HEAs. In this investigation, there were mixed microstructure. Moreover, the constituent phases of the microstructures changed from (FCC + BCC1) phases to (BCC1 + BCC2 + intermetallic compound) phases with the increasing of Ti content from Ti_0 alloy to $Ti_{1.5}$ alloy. Ti-containing intermetallic compounds were even obtained in the $Ti_{1.0}$ and $Ti_{1.5}$ alloy. Qi and Chrzan pointed out that there were two aspects about alloy's ductility that should be considered during alloy design [25]. One was so-called extrinsic features of the alloy, for example, grain size and precipitate distribution, etc. The other was the intrinsic ductility of its perfect crystal. The ductility of the investigated HEAs in this paper did not improve with the decreasing of VEC which seemed that there was a contradiction with the previous researches; however, more attentions should be paid on the mixed microstructure and the formation of Ti-containing intermetallic compounds. From those perspectives, it could be deduced that the extrinsic features played more important roles on the ductility rather than the intrinsic ductility in this investigation.

Figure 7 showed the fracture morphologies of $Ti_{0.5}$, $Ti_{1.0}$ and $Ti_{1.5}$ alloys, and the Ti_0 alloy did not parted. It could be seen from Fig. 7a that tearing ridges were observed in the fracture surface of the $Ti_{0.5}$ alloy, indicating the alloy had a certain degree of plasticity. The cleavage steps and the river patterns formed by the tearing process of the cleavage steps could be observed at the fracture surface of $Ti_{1.0}$ alloy, and the fracture surface was relatively flat, indicating cleavage brittle fracture was dominated in the $Ti_{1.0}$ alloy as shown in Fig. 7b. The cleavage steps could be also observed at the fracture surface of $Ti_{1.5}$ alloy shown in Fig. 7c, and its fracture surface was flatter than that of $Ti_{1.0}$ alloy, indicating the plasticity of the $Ti_{1.5}$ alloy was worse than that of $Ti_{1.0}$ alloy. It could be confirmed from the fracture morphologies that the $Ti_{0.5}$ alloy had the best plasticity while the $Ti_{1.5}$ alloy
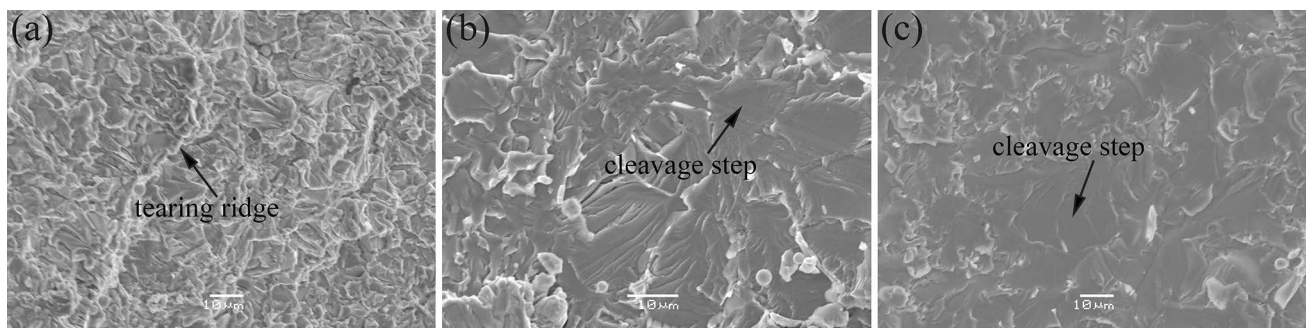

Fig. 7 Fracture surface morphologies of the $Ti_{0.5}$ alloy (**a**), $Ti_{1.0}$ alloy (**b**) and $Ti_{1.5}$ alloy (**c**)

had the highest brittleness which was consistent with the compression curve. The compressive strength of the alloys was increased and the compression ratio was reduced by the addition of an appropriate amount of Ti element. On the one hand, the addition of Ti atoms as the solute atoms imposed the pinning effect to the dislocations and also hindered the movement of dislocations. Moreover, the larger lattice distortion caused by the large difference of atomic radius making the dislocation difficult to move, thereby increasing the compressive strength and reducing the plasticity. On the other hand, a large amount of BCC phase was formed in the alloys with the increasing of Ti content, whereas, the plastic deformation ability of BCC phase was worse than that of the FCC phase. In addition, Ti-containing intermetallic compound was distributed on the grain boundary in the $Ti_{1.5}$ alloy, aggravating the local stress concentration during the process of brittle deformation which promoted the production and growth of the cracks. Finally, a large number of cleavage steps were formed on the fracture surface of the $Ti_{1.5}$ sample.

5 Conclusions

1. The predictions of the empirical parameters were basically in agreement with the experimental results in the investigated $Al_{0.5}CrFeMn_{0.8}Ni_{2.1}Ti_x$ alloys. The predicted parameters of the $Ti_{1.5}$ alloy were near the critical values indicating the alloy had a obvious tendency to form intermetallic compound, which was consistent with the experimental results.

2. The addition of Ti elements promoted the formation of BCC phase in $Al_{0.5}CrFeMn_{0.8}Ni_{2.1}Ti_x$ alloys. In addition to the BCC1 phase and BCC2 phase, Fe_2Ti intermetallic compound was even obtained in $Ti_{1.5}$ alloy. Moreover, chrysanthemum-like eutectic microstructure appeared in the $Ti_{0.5}$ and $Ti_{1.0}$ alloys. The flower core was composed of BCC2 phase and eutectic microstructure was achieved in the petal which contained BCC1 phase and BCC2 phase. In the $Ti_{1.5}$ alloy, the eutectic microstructure disappeared because of the appearance of divorced eutectic.

3. The macrohardness increased with the increasing of Ti content, while the compressive maximum stress and the plasticity of the broken $Al_{0.5}CrFeMn_{0.8}Ni_{2.1}Ti_x$ alloys decreased with the increasing of Ti content. The $Ti_{0.5}$ alloy had the best combination of plasticity and compressive strength, and its compressive maximum stress was reached to 1523 MPa and the compressive strain to fracture was about 5.6%.

References

1. J.W. Yeh, S.K. Chen, S.J. Lin, J.Y. Gan, T.S. Chin, T.T. Shun, C.H. Tsau, S.Y. Chang, Adv. Eng. Mater. **6**, 299 (2004)
2. C.Y. Hsu, C.C. Juan, T.S. Sheu, S.K. Chen, J.W. Yeh, JOM **65**, 1840 (2013)
3. C.P. Tang, X.Z. Wang, W.H. Liu, D. Feng, K. Wu, C. Zhang, G.D. Miao, W.Y. Liang, J. Li, X. Liu, Q. Li, Mater. Sci. Eng. A **759**, 172 (2019)
4. X. Chen, D. Gao, J.X. Hu, Y. Liu, C.P. Tang, Met. Mater. Int. **25**, 1135 (2019)
5. J.W. Yeh, Y.L. Chen, S.J. Lin, S.K. Chen, Mater. Sci. Forum **560**, 1 (2007)
6. F. Peyrouzet, D. Hachet, R. Soulas, C. Navone, S. Godet, S. Gorsse, JOM **71**, 3443 (2019)
7. W. Zhang, P.K. Liaw, Y. Zhang, Sci. China Mater. **61**, 2 (2018)
8. Z. Li, K.G. Pradeep, Y. Deng, D. Raabe, C.C. Tasan, Nature **534**, 227 (2016)
9. X. Chen, S.D. Zhai, D. Gao, J. Xu, Y. Liu, Y. Liu, F.C. Yin, J Mater. Eng. Perform. **28**, 4502 (2019)
10. H. Luo, Z. Li, A.M. Mingers, D. Raabe, Corros. Sci. **134**, 131 (2018)
11. J.Y. He, W.H. Liu, H. Wang, Y. Wu, X.J. Liu, T.G. Nieh, Z.P. Lu, Acta Mater. **62**, 105 (2014)
12. B. Gludovatz, A. Hohenwarter, D. Catoor, E.H. Chang, E.P. George, R.O. Ritchie, Science **345**, 1153 (2014)
13. D.Y. Li, C.X. Li, T. Feng, Y.D. Zhang, G. Sha, J.J. Lewandowski, P.K. Liaw, Y. Zhang, Acta Mater. **123**, 285 (2017)
14. B.S. Li, Y.P. Wang, M.X. Ren, C. Yang, H.Z. Fu, Mater. Sci. Eng. A **498**, 482 (2008)
15. B. He, N.N. Zhang, D.Y. Lin, Y. Zhang, F.Y. Dong, D.Y. Li, Coatings **7**, 157 (2017)
16. H.Y. Chen, C.W. Tsai, C.C. Tung, J.W. Yeh, T.T. Shun, C.C. Yang, P.H. Lee, Eur. J. Control **31**, 685 (2006)
17. S.K. Wong, T.T. Shun, C.H. Chang, C.F. Lee, Mater. Chem. Phys. **210**, 146 (2018)
18. Y.P. Lu, Y. Dong, S. Guo, L. Jiang, H.J. Kang, T.M. Wang, B. Wen, Z.J. Wang, J.C. Jie, Z.Q. Cao, H.H. Ruan, T.J. Li, Sci. Rep. **4**, 6200 (2014)
19. M.A. Hemphill, T. Yuan, G.Y. Wang, J.W. Yeh, C.W. Tsai, A. Chuang, P.K. Liaw, Acta Mater. **60**, 5723 (2012)
20. Y. Zhang, Y.J. Zhou, J.P. Lin, G.L. Chen, P.K. Liaw, Adv. Eng. Mater. **10**, 534 (2008)
21. Y. Zhang, T.T. Zuo, Z. Tang, M.C. Gao, K.A. Dahmene, P.K. Liaw, Z.P. Lu, Prog. Mater. Sci. **61**, 1 (2014)
22. S. Guo, C. Ng, J. Lu, C.T. Liu, J. Appl. Phys. **109**, 103505 (2011)
23. X. Yang, Y. Zhang, Mater. Chem. Phys. **132**, 233 (2012)
24. S. Sheikh, S. Shafeie, Q. Hu, J. Ahlström, C. Persson, J. Veselý, J. Zýka, U. Klement, S. Guo, J. Appl. Phys. **120**, 164902 (2016)
25. L. Qi, D.C. Chrzan, Phys. Rev. Lett. **112**, 115503 (2014)
26. H.W. Yao, J.W. Qiao, J.A. Hawk, H.F. Zhou, M.W. Chen, M.C. Gao, J. Alloys Compd. **696**, 1139 (2017)
27. H.W. Yao, J.W. Qiao, M.C. Gao, J.A. Hawk, S.G. Ma, H.F. Zhou, Y. Zhang, Mater. Sci. Eng. A **674**, 203 (2016)